J. Mech. Phys. Solids 206 (2026) 106403

Contents lists available at ScienceDirect

Journal of the Mechanics and Physics of Solids

journal homepage: www.elsevier.com/locate/jmps

# Non-reciprocal three-dimensional mechanical metamaterials

Qingxiang Ji [a,1], Jinliang Wang [b,1], Brahim Lemkalli [a], Gwenn Ulliac [a], Changguo Wang [b,*], Sébastien Guenneau [c,d], Muamer Kadic [a,*]

[a] Université Marie et Louis Pasteur, Institut FEMTO-ST, 25000 Besançon, France
[b] National Key Laboratory of Science and Technology on Advanced Composites in Special Environments, Harbin Institute of Technology, Harbin, 150001, PR China
[c] UMI 2004 Abraham de Moivre-CNRS, Imperial College London, SW7 2AZ, London, UK
[d] The Blackett Laboratory, Physics Department, Imperial College London, SW7 2AZ, London, UK

ARTICLE INFO

*Keywords:*
Non-reciprocity
Mechanical metamaterials
Elastic modulus
Dispersion
Band-gaps

ABSTRACT

Mechanical metamaterials have recently driven significant advancements, and this field has currently been extended to break the reciprocity principle in static mechanics and wave propagation. Here, we demonstrate a type of three-dimensional mechanical metamaterials that possess nonreciprocal static elastic behaviors and tunable dynamic wave properties. The metamaterial is designed with suitably tailored microstructure asymmetry, which exhibits vastly different deformation configurations upon loading from different sides. Such contrast in deformation induces distinct force–displacement responses, which gives nonlinear elastic moduli that are dependent on both the magnitude and direction of applied loads. We fabricate such metamaterials with 3D printing technique at the microscale. The non-reciprocal mechanical behavior is validated by analytical means, simulations, and experiments. Besides, tunable band structure characteristics are obtained when the metamaterial is loaded in opposite directions or by different magnitudes. The band structure deforms in asymmetrical ways, which indicates flexible control on transmit–prohibit switching of elastic waves propagation (in certain frequency ranges), and this is realized by only switching the external mechanical loading direction. These peculiar behaviors show great prospects in enabling unidirectional elasticity and wave transmission within a solid material, paving avenues to new one-way functional devices.

## 1. Introduction

Mechanical metamaterials reshape the physical property boundaries of solid materials and display rich extraordinary characteristics in both static and dynamic regimes (Florijn et al., 2014; Frenzel et al., 2017; Kadic et al., 2019; Reis et al., 2015; Ji et al., 2021; Surjadi et al., 2019; Chen et al., 2021; Li et al., 2023; Hu et al., 2023; Ni et al., 2024; Wang et al., 2025). Recently mechanical metamaterials have been extended to the non-reciprocal regime that goes beyond the Maxwell–Betti reciprocity theorem. The law of reciprocity indicates that the signal propagates in symmetrical manner through a material or a system. Non-reciprocal metamaterials can generate asymmetrical transmission of signal or energy between two space locations when only switching the propagating directions. Note that the Maxwell–Betti reciprocity theorem is derived under some basic assumptions including the fact that the system under analysis is linear, which implies a path to obtain non-reciprocity by breaking these limitations. If homogeneous

* Corresponding authors.
*E-mail addresses:* wangcg@hit.edu.cn (C. Wang), muamer.kadic@univ-fcomte.fr (M. Kadic).
[1] These authors contributed equally to this work.

https://doi.org/10.1016/j.jmps.2025.106403
Received 12 May 2025; Received in revised form 12 October 2025; Accepted 14 October 2025
Available online 24 October 2025

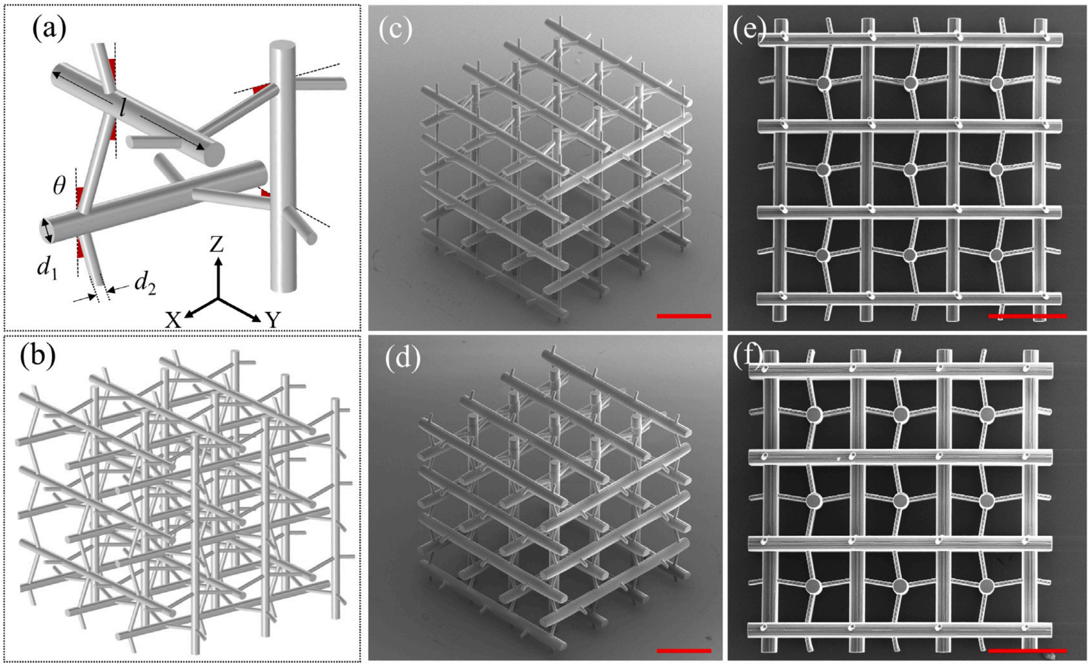


**Fig. 1.** Structure design of the nonreciprocal mechanical metamaterial. (a) Unit cell and (b) an array composed of 3 × 3 × 3 unit cells. (c, d) Scanning electron micrograph of the micro-lattice samples fabricated via direct laser writing technology: they are same structures but with opposite up-and-down order. Panels (e, f) show the samples from the top view. In all panels, the scale bars denote 50 μm.

and isotropic constituents are used, a nonreciprocal structure often meets two requirements: asymmetrical geometry and nonlinear deformation. Asymmetrical geometry is obvious in the sense that different responses can be generated upon switching directions. In addition, Maxwell–Betti reciprocal law states that a mechanical structure (either symmetrical or asymmetrical) is reciprocal in its linear stage. Therefore, suitably introducing nonlinearity is another necessary condition to achieve non-reciprocity (Lamb, 1887; Achenbach, 2003; Li et al., 2024).

For most natural elastic materials, their corresponding coefficients (e.g., Young's modulus) are often independent of the load conditions. By contrast, nonreciprocal mechanical metamaterials can exhibit different elasticities in tension and compression. This paves new avenues in directing, controlling, and modulating mechanical signals and energy in ways that are previously impossible in the reciprocal regime. Furthermore, as non-reciprocal mechanical metamaterials can exhibit different elasticities at different load conditions, they have significant potentials as diodes, rectifiers or topological insulators (Nadkarni et al., 2016; Librandi et al., 2021; Trainiti and Ruzzene, 2016; Süsstrunk and Huber, 2015; Attarzadeh and Nouh, 2018; Attarzadeh et al., 2019).

To date, non-reciprocity is mostly realized in dynamic regime by breaking the time-reversal symmetry with the help of external excitation, active materials or changing boundary conditions (Wang et al., 2015; Nassar et al., 2020; Palermo et al., 2020; Xu et al., 2020; Zhang et al., 2021). In static mechanics, non-reciprocity is less investigated and is often activated by asymmetrical microstructures that induce distinct deformations along different loading directions. In 2017, Coulais et al. first proposed the concept of static non-reciprocity in 2D metamaterials using fish-bone microstructures (Coulais et al., 2017). Their developed metamaterials exhibit vastly different output displacements under excitation from various sides, as well as one-way displacement amplification. Consequently, static nonreciprocity was further developed to non-reciprocal elastic moduli (Shaat et al., 2020; Shaat, 2020; Shaat and Park, 2023), shock resistance (Wang et al., 2023b), Janus property with plug-switch orientation (Zhang et al., 2024), self-regulated non-reciprocal motions (Li et al., 2022), etc. Apart from 2D lattice structures, recently researchers have explored static non-reciprocity in 3D metamaterials, e.g., 3D chiral metamaterials with Poynting effects (Dong et al., 2024) and asymmetric elasticity (Montazeri et al., 2025), composite hydrogels with asymmetrical shear responses (Wang et al., 2023a).

Motivated by the design path of asymmetrical deformation modes, here we demonstrate a new 3D mechanical meta-structure that is capable of transferring deformation in a non-reciprocal manner. The metamaterial shows asymmetrical mechanical responses and its elastic modulus depends on both the magnitude and direction of the applied force. An analytical model is established to capture the nature of asymmetrical deformation patterns and their resulting non-reciprocal force–displacement responses. Microscale metamaterial samples are fabricated by 3D printing technology, and the non-reciprocal properties are verified by means of experimental and simulated analysis. We also study the band structures of elastic waves in the proposed metamaterial, where the asymmetric deformation induces strong difference between the first band gap characteristics.

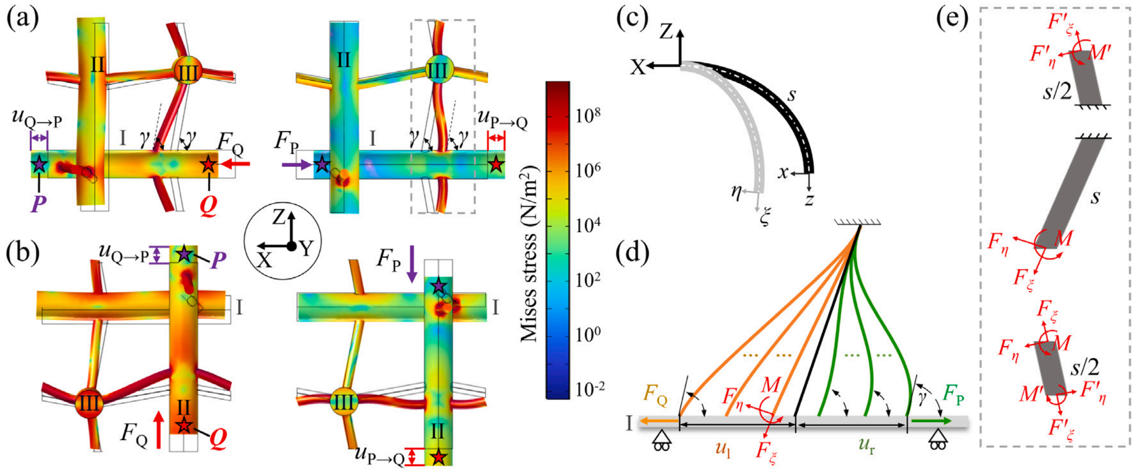


**Fig. 2.** Deformation and Mises stress profile of the mechanical metamaterial with external forces exerted on opposite ends along (a) $x$-axis and (b) $z$-axis, respectively. The direction-dependent deformation patterns will give rise to nonreciprocal behavior in the static state and elastic waves. The black lines depict the pristine configuration of the structure. (c) The coordinate systems employed for a beam with initial bending curvature, where $xoz$ and $\xi o \eta$ describe the pristine and deformed shapes, respectively. (d) The force state of a representative connector beam. (e) Force analysis of representative connector beams which are attached to a base beam under applied loads.

## 2. Metamaterial design

We depict the features of proposed 3D mechanical metamaterials in Fig. 1(a, b). The unit cell, with a uniform spatial period of $l$ = 100 μm, is composed of base beams and tilt connectors whose diameters are $d_1$ = 19.25 μm and $d_2$ = 5.5 μm, respectively. In the asymmetrical configuration, all the connectors undergo a rotation of $\theta = 10°$ with regard to the base beam's normal. This inclination angle $\theta$ is defined as the angle between the base beams and the inclined connectors (ranging from 0 to 90°), which serves the purpose of introducing asymmetry within the structure. Nonreciprocity in the elastic modulus is induced by tilting the connectors with respect to the base beam's normal. When $\theta = 0$, the structure becomes axially symmetric, corresponding to the symmetric case. The elastic non-reciprocity is dependent on the geometrical asymmetry, where the angle $\theta = 0$ can be used to tailor the intensity of non-reciprocity.

We have fabricated two sets of samples with polymers using two-photon lithography 3D Direct Laser Writing (Photonic Professional GT+, Nanoscrible GmbH), as shown in Fig. 1(c–f). The two sets of samples have opposite up-and-down order so that compressive loading is always implemented from the top end during the mechanical testing. The customized commercial negative tone IP-S resin (Nanoscrible GmbH) was employed as the raw material which has a density of $\rho$ = 1200 kg m$^{-3}$, a Poisson ratio of $\nu$ = 0.4 and a Young modulus of $E$ = 3 GPa. A drop of IP-S resin was deposited on an ITO-coated glass substrate with dimensions 25 mm × 25 mm × 0.7 mm and photo-polymerized with a femtosecond laser operating at $\lambda$ = 780 nm and an objective of 25×. After printing, the samples were developed for 30 min in propylene glycol methyl ether acetate (PGMEA) solution to remove the unexposed photoresist and rinsed for 5 min in Isopropyl alcohol (IPA) to clear the developer. A laser power of 100 mW and a galvanometric scan speed of 100 mm/s were used for the whole fabrication process.

## 3. Results and discussion

### *3.1. Asymmetrical structural deformation*

We present the different deformation patterns of the developed metamaterials under mechanical stimuli from different directions in Fig. 2. The base beams are designed with larger sizes than the connectors to minimize their buckling and generate quasi-rigid movement when the structure encounters external loads. The inclination of the connectors induces different types of promotion on the base beams to move following external forces, thus generating deformation asymmetries. It is observed that the connectors undergo significant buckling when pushed from the left end P (i.e., loading condition $F_P$) while showing minor deflection when pushed from the right end Q (i.e., loading condition $F_Q$), as shown in Fig. 2(a). Such asymmetrical deformation profiles will promote different force–displacement responses that imply elastic non-reciprocity. The contrast in the deformation patterns can be attributed to the difference in force states in the structure. When an external force $F_P$ (or $F_Q$) acts on the end P (or Q) of base beam, it decomposes into two components, i.e., axial force $F_P \sin\theta$ (or $F_Q \sin\theta$) and transverse force $F_P \cos\theta$ (or $F_Q \cos\theta$). Because of these two force components, the tilt connector exhibits a combined deformation of transverse deflection and axial compression/tension. In one direction, the structure is deflected and stretched; in the opposite direction, the structure is deflected and compressed to buckling. The asymmetrical deformation and stress states are depicted in Fig. 2(a, b). This contrast leads to different axial displacements of the structure upon switching the direction of the applied force. Even if the magnitude is kept unchanged, the opposite direction forces produce different displacements.

Note that we take the deformation in $xoz$ plane as a typical case to show the mechanical response characteristics. A displacement $u_{P\to Q}$ on the right end Q is generated when the structure is pushed from the left end P (indicated as loading condition $F_P$). Similarly, a displacement $u_{Q\to P}$ is generated on the left end P when pushed from the right end Q (indicated as loading condition $F_Q$). One can certainly investigate the behavior from the $yoz$ and $xoy$ plane views, as the same phenomenon will be observed thanks to the rotary geometry similarity. Even in the considered $xoz$ view, one can actually recover the load conditions depicted in Fig. 2a by flipping and rotating the view in panel Fig. 2b. This characteristic will be further clarified in subsequent results.

To derive more insights into the asymmetrical deformation profiles and force states, we develop an analytical model. We start from force analysis and deformed configurations on a typical element which is composed with a base beam and a tilt connector, as depicted in Fig. 2d. Here beam III is fixed and beam I is encountered with external forces. Upon forces from different ends (e.g. $F_x$), the base beam is moved rigidly and the free end is translated by $\mu_l$ or $\mu_r$ along the horizontal direction with invariant tilt angle $\gamma$ with respect to the base beam. Here $\gamma = (90° - \theta)$ is the complementary angle of $\theta$ and it is used for more convenient depiction. We should note that in the first-step movement of the base beam, the tilt beams deform from a straight state to bending/buckling configurations; in subsequent steps, force analysis on the tilt beam should start from its curved configuration with initial stress/strain taken into consideration. Therefore, a geometrically exact beam model is employed here, which considers the initial extension–bending coupling of the tilt connectors and is thus closer to the true stress state. We realize that such a model can accurately capture the deformation of three-dimensional curved beams; however, here it is simplified to a two-dimensional form as the tilted connectors deform in a plane face approximately.

The model is described by three sets of coordinates, as depicted in Fig. 2c. The global coordinate system XOZ is fixed to the ground and is used as a reference for initial curvatures. The system $xoz$ describes the shape of undeformed beams, where axis $z$ depicts the reference line of the beam. Here $\mathbf{i}_x$, $\mathbf{i}_z$ are employed as the unit vectors along axis $x$, $z$, respectively. We have

$$\frac{\mathrm{d}}{\mathrm{d}s}\begin{bmatrix}\mathbf{i}_z\\ \mathbf{i}_x\end{bmatrix} = \mathbf{k}\begin{bmatrix}\mathbf{i}_z\\ \mathbf{i}_x\end{bmatrix}, \tag{1}$$

where $s$ is the initial arc length of the bent beam. The matrix $\mathbf{k}$ is the initial curvature matrix which represents the derivative of unit vectors $\mathbf{i}_z$ and $\mathbf{i}_x$ along the axes $z$ and $x$ with respect to $s$, and is expressed as

$$\mathbf{k} = \begin{bmatrix}0 & k\\ -k & 0\end{bmatrix} \tag{2}$$

with $k$ denoting the initial bending curvature.

Similarly, the coordinate system $\xi o\eta$ describes the shape of deformed beams, where axis $\xi$ denotes the reference line of the beam. Here $\mathbf{i}_\xi$, $\mathbf{i}_\eta$ are used as the unit vectors along axis $\xi$, $\eta$, respectively. We have

$$\frac{\mathrm{d}}{\mathrm{d}s}\begin{bmatrix}\mathbf{i}_\xi\\ \mathbf{i}_\eta\end{bmatrix} = \mathbf{K}\begin{bmatrix}\mathbf{i}_\xi\\ \mathbf{i}_\eta\end{bmatrix}. \tag{3}$$

The matrix $\mathbf{K}$ is the deformed curvature matrix which represents the derivative of unit vectors $\mathbf{i}_\xi$ and $\mathbf{i}_\eta$ along the axes $\xi$ and $\eta$ with respect to $s$. $\mathbf{K}$ is expressed by

$$\mathbf{K} = \begin{bmatrix}0 & \rho\\ -\rho & 0\end{bmatrix}, \tag{4}$$

where $\rho$ denotes the bending curvature of the deformed beam.

Both $\xi o\eta$ and $xoy$ are orthogonal curvilinear coordinate systems, and they are correlated by the transformation matrix $\mathbf{T}$

$$\begin{bmatrix}\mathbf{i}_\xi\\ \mathbf{i}_\eta\end{bmatrix} = \mathbf{T}\begin{bmatrix}\mathbf{i}_z\\ \mathbf{i}_x\end{bmatrix} = \begin{bmatrix}T_{11} & T_{12}\\ T_{21} & T_{22}\end{bmatrix}\begin{bmatrix}\mathbf{i}_z\\ \mathbf{i}_x\end{bmatrix}, \tag{5}$$

where $T_{ij}$ denote elements of the transformation matrix $\mathbf{T}$ which are expressed by

$$T_{11} = T_{22} = \frac{1 + w' - uk}{1+\epsilon}, T_{12} = \frac{u' + wk}{1+\epsilon}, T_{21} = \frac{-u' - wk}{1+\epsilon}. \tag{6}$$

Here $u, w$ are the displacements of the beam end with respect to axes $z, x$, and $\epsilon$ is the axial strain on the reference line. The symbol $()' = d()/ds$ is used with respect to system $\xi o\eta$.

Differentiating Eq. (5) and combining it with Eq. (1), we get

$$\frac{\mathrm{d}}{\mathrm{d}s}\begin{bmatrix}\mathbf{i}_\xi\\ \mathbf{i}_\eta\end{bmatrix} = \left(\frac{\mathrm{d}\mathbf{T}}{\mathrm{d}s} + \mathbf{Tk}\right)\begin{bmatrix}\mathbf{i}_z\\ \mathbf{i}_x\end{bmatrix} = \left(\frac{\mathrm{d}\mathbf{T}}{\mathrm{d}s} + \mathbf{Tk}\right)\mathbf{T}^{-1}\begin{bmatrix}\mathbf{i}_\xi\\ \mathbf{i}_\eta\end{bmatrix}, \tag{7}$$

We then substitute Eq. (7) into Eq. (3) to obtain

$$\frac{\mathrm{d}\mathbf{T}}{\mathrm{d}s} = \mathbf{KT} - \mathbf{Tk} \tag{8}$$

The force on the free end is decomposed into two force components $F_\xi$ and $F_\eta$ and one moment of magnitude $M$. Note that all the forces, moments, rotations and displacements are functions of the variable $s$, which indicates the undeformed arc length of the beam. Specifically, we have the following governing equations for the forces (Pai and Nayfeh, 1994; Pai and Palazotto, 1996)

$$\begin{cases} \dfrac{\mathrm{d}\mathbf{F}}{\mathrm{d}s} + \mathbf{K}^{\mathrm{T}}\mathbf{F} = \mathbf{0} \\ \dfrac{\mathrm{d}M}{\mathrm{d}s} - (1+\epsilon)F_\eta = 0 \end{cases} \tag{9}$$

where $\epsilon$ indicates axial strain, $\mathbf{F} = [F_\xi, F_\eta]^{\mathrm{T}}$ denotes stress resultant in system $\xi o \eta$, and $M$ is stress moment around the axis perpendicular to system $\xi o \eta$. The displacements are determined by

$$\frac{\mathrm{d}\mathbf{u}}{\mathrm{d}s} = \mathbf{k}\mathbf{u} + (1+\epsilon)\begin{bmatrix} T_{11} \\ T_{12} \end{bmatrix} + \begin{bmatrix} -1 \\ 0 \end{bmatrix} \tag{10}$$

where $\mathbf{u} = [w, u]^{\mathrm{T}}$ indicates the displacements with respect to the axes $z, x$.

Considering that $T_{11}^2 + T_{12}^2 = 1$, we have 6 unknown variables in total, i.e., $F_\xi$, $F_\eta$, $M$, $T_{11}$, $w$, $u$ in the governing equations (Pai and Palazotto, 1996). The boundary conditions of flexible beams are

$$\delta\mathbf{u} = 0, \delta\theta = 0, \tag{11}$$

where $\theta$ is rotation around axis $\eta$ and $\delta\theta$ ($\delta\mathbf{u}$) is virtual rotation (displacement). The force state of tilt beams is shown in Fig. 2d, where one end (fixed end) is fixed on the ground and another end (free end) is fixed on the horizontal base beam. When a force is applied on the base beam, the free end of the tilt connector is translated (indicated by $u_l$ or $u_r$) along the horizontal direction and retains its tilt angle, which indicates that it is subjected to two forces $F_z$, $F_x$, and one moment $M$. The boundary condition of the fixed end is

$$\begin{cases} T_{11} = 1 \\ u = w = 0 \end{cases} \tag{12}$$

The boundary condition of the free end is

$$\begin{cases} T_{11} = 1 \\ w = u_{l(r)} \sin\theta \\ u = u_{l(r)} \cos\theta \end{cases} \tag{13}$$

We emphasize again that all the forces, moments, rotations, and displacements are functions of the undeformed arc length of the beam. In the periodic cell of our proposed metamaterials, we note that the base beam is attached with tilt connector beams of different arc length on its two sides ($s$ or $s/2$). One can obtain the mechanical forces $F'_\xi$, $F'_\eta$, $M'$ by substituting different arc lengths and boundary conditions into the above equations (the top panel in Fig. 2e). However, the same set of mechanical forces $F_\xi$, $F_\eta$, $M$ will be retrieved at the end of the base beam due to periodic conditions (the bottom panel in Fig. 2e). Therefore, the integral force on the end of beam I is approximately presented by $F_e = 4F_t$, where $F_e$ is the force subjecting to base beam, $F_t$ is the component of $\mathbf{F}$ driving beam I to move. Besides, beam II will be deflected and will contribute to the displacement of beam I. However, such influence is safely ignored in the analytical model due to the large contrast of diameters (and thus bending stiffness) between the base beam and the tilt connector.

In order to solve Eqs. (9) and (10), which are ordinary differential equations with two-point boundary values, we use the multiple shooting method. Note that the Jacobi matrix exhibits singularity as the initial curvature of the tilt connector is 0. This singularity will break the iteration process. Here we propose a revised method where the straight beam is replaced by a micro-bending beam with enough small initial curvature $k$ to approximate a straight one. The properties of micro-bending beams are the same as those of straight beams with initial curvatures. We use a micro-bending beam with a small (even to the degree of negligible curvature, e.g., $R = 1/k = 1000$ μm) instead of straight beams to compute the force–displacement relation of the proposed structure. As shown in Fig. 3a, the relation curve indicates that the tilt beams are unstable when they are pushed from the left end (P) whereas they are not when pushed from the right end (Q). It shows an apparent difference between opposite directions, which can result in the non-reciprocity of the metamaterials. The good agreement between theoretical and Finite Element Method (FEM) results validates the accuracy of the developed theory model (Fig. 3a, b). We obtain identical force–displacement responses when the lattice structure is loaded in $x$ direction and $z$ direction, which is due to the rotational geometry similarity (Fig. 3c). With this phenomenon in mind, in subsequent sections we only investigate the mechanical behavior with the compressive loading implemented in the $z$ direction.

### 3.2. Non-reciprocity in static mechanics

We move to experimental and numerical investigation on the non-reciprocal mechanical behavior of the designed metamaterial lattices under compressive deformation. For the 3D micro-scale samples used in the testing (Fig. 4), the lattice structures and the fixed boundaries (realized by two side blocks) were printed from the bottom to the top. In the compressive deformation tests, the loads are applied on opposite ends of the metamaterial lattices in sequence. Home-made experimental setup was built and used, which could characterize static mechanical behaviors at the microscale. The setup consists of a flat compression stage, a force sensor, a digital camera equipped with a 50× objective lens, an LED light, and a computer. The whole setup works in a dark environment, and the only source of light is the LED. In this way, the 50× objective can capture the deformation configurations of the samples. Specifically, the samples were placed between a fixed glass substrate and the compression stage. The stage was driven by a stepping

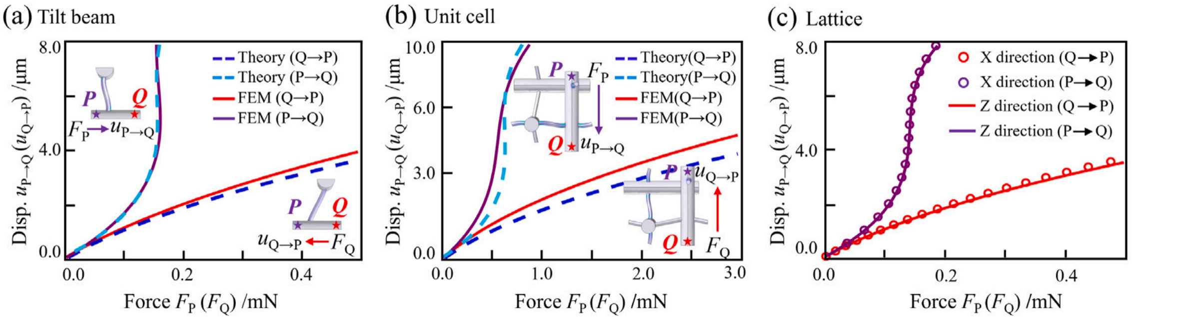


**Fig. 3.** Nonreciprocal mechanical responses for (a) a tilt connector beam, (b) a unit cell, and (c) an array composed of 3 × 3 × 3. Results in panel (c) are obtained by FEM, which depicts the identical mechanical responses when loaded in different directions. For clarity, in the inserts we denote the different loading conditions.

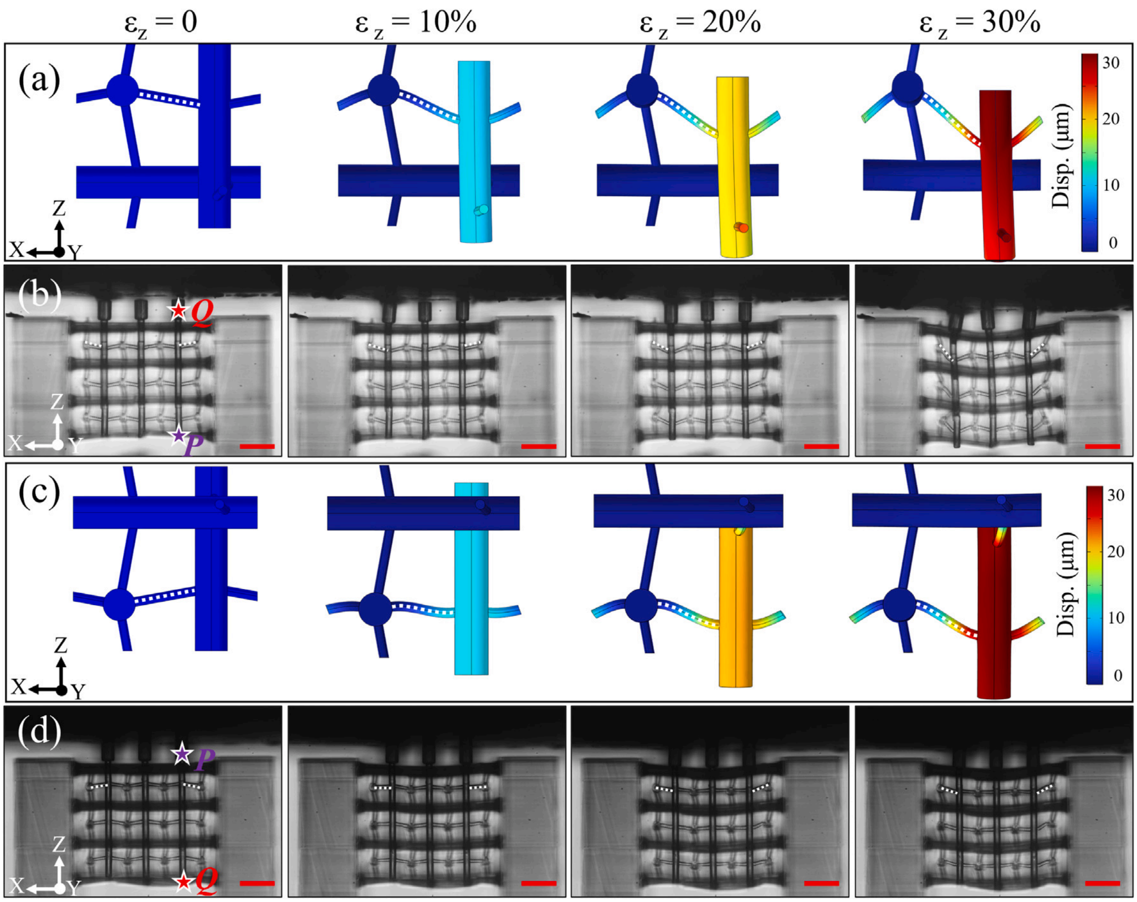


**Fig. 4.** Experimental and simulated demonstration of the non-reciprocal deformation of the metamaterial. (a) Simulated and (b) experimental results for compressive deformations under different strains $\varepsilon_z$, which corresponds to the loading situation $F_Q$. (c, d) Same as panels (a, b), but corresponds to the loading situation $F_P$. In all panels, the deformation of the tilt connector beam is marked by the white line.

motor with the force sensor attached. During the testing, we applied compressive displacements of 30 μm on the samples via the stage. Force–displacement responses were obtained and recorded by the sensing device and then displayed on the computer. Note that the position was directly read from the stage, but was only used to monitor the deformation of the structure. The true strain was obtained via subsequent image cross-correlation analysis. The compression was divided into 30 steps with each step being 1 μm, and it was carried out at a speed of 1 μm/s. For numerical simulations, the commercial software Abaqus 2025 was employed. Identical 3D geometry models were built for simulations and for 3D printing to reduce the difference between experiments and simulations.

The lattice structures were fixed at left/right sides while compressive displacement was applied on the top end. Specifically, in the "Interaction" section, we created reference points that are coupled with all top-end surfaces. In the coupling, the reference point constrained all degrees of freedom of the top ends. Then compressive displacement is applied to the reference point. Finally, in the "Results" section, the surface integration sub-option under the derived values was employed to output the reaction force in the $z$-direction.

To reveal the nature of variations of the elastic constants under different-direction loading, the deformations are reported in Fig. 4 for different compressive strains $\varepsilon_z$, i.e., $0, 10\%, 20\%$ and 30%, respectively. We apply compressive input displacements on the samples, then measure and record corresponding reaction forces. The reaction force is divided by the cross-section of the samples to compute the effective stress $\sigma_z$, and the deformation between top and bottom boundary surfaces, divided by the $z$-direction size of the samples, is employed to indicate effective strain $\varepsilon_z$. It is worth noting that the tilt connectors undergo buckling–compression coupling in one direction while encountering bending-stretching in another direction, as marked by the white lines in Fig. 4. The deformed shapes obtained from simulations are generally in good agreement with experimental results. This asymmetrical deformation is the key element that produces non-reciprocal elastic constants. As a note, in the experimental testing, the samples are fixed to blocks on two sides to produce fixed boundary conditions, while in simulations, periodic boundary conditions are implemented on the unit cell. This induces the discrepancy of deformed configurations (and subsequent mechanical responses) between simulations and experiments, especially for the unit cells located in the inner domain of the lattices. However, the results are convincing enough for our proof-of-concept demonstration.

Distinct force–displacement responses are observed for opposite loading directions in Fig. 5a. The good agreement between experimental and FEM results validates the effectiveness of our proposed design. We mention in passing that the discrepancies between experiments and simulations are mainly attributed to imperfections in fabrications, testing errors, and differences of applied boundary conditions (as depicted above). Besides, the computational model only considers geometric non-linearity of the metamaterials, while the plasticity of the constitutive material is ignored. Further insight into the nonreciprocal property is obtained by studying the nonreciprocity of material deformation using

$$\alpha = \frac{|F_{\mathrm{P}} u_{\mathrm{Q}\to\mathrm{P}} - F_{\mathrm{Q}} u_{\mathrm{P}\to\mathrm{Q}}|}{F_{\mathrm{P}} u_{\mathrm{Q}\to\mathrm{P}} + F_{\mathrm{Q}} u_{\mathrm{P}\to\mathrm{Q}}}, \tag{14}$$

where $F_{\mathrm{P}}$ and $F_{\mathrm{Q}}$ denote the magnitudes of reaction forces obtained from P and Q end, respectively; $u_{\mathrm{P}\to\mathrm{Q}}$ and $u_{\mathrm{Q}\to\mathrm{P}}$ are displacements induced at their corresponding opposite ends. Note that we take the scalar value of all forces and displacements for clarity. According to Eq. (14), the metamaterial exhibits symmetrical deformations and obeys $\alpha = 0$. By contrast, asymmetrical deformations and generally nonlinear elastic material behavior will be presented if $\alpha \neq 0$. Note that deformation non-reciprocity is often characterized by displacement/strain differences produced by applying forces with the same magnitude but opposite directions (Coulais et al., 2017; Shaat et al., 2020). In our experiments and simulations, we apply compressive displacements instead, thus, the reaction forces are employed to demonstrate deformation non-reciprocity. As depicted in Fig. 5b, obvious deformation non-reciprocity is observed throughout the compression process, and the non-reciprocity parameter is not constant but robustly dependent on the applied compressive strains.

We then consider the energy absorption behavior of the lattice structures along opposite loading directions. The energy absorption behavior is studied by the mechanical work, which is defined as the work performed by the uniaxial compression force $F_{\mathrm{P}}$ (or $F_{\mathrm{Q}}$) at P (or Q) end, up to the deformation displacement $u_{\mathrm{P}}$ (or $u_{\mathrm{Q}}$) taken as a magnitude of 30 μm, and is expressed as (Chen et al., 2022b,a; Zhang et al., 2025)

$$W_{\mathrm{P}} = \int F_{\mathrm{P}} \cdot du_{\mathrm{P}} \quad \left(W_{\mathrm{Q}} = \int F_{\mathrm{Q}} \cdot du_{\mathrm{Q}}\right). \tag{15}$$

Here we use $W_{\mathrm{P}}$ and $W_{\mathrm{Q}}$ to denote the mechanical work corresponding to different loading directions, respectively; $u_{\mathrm{P}}$ and $u_{\mathrm{Q}}$ are the input displacements at the end that the compression force is applied. An obvious energy absorption difference is observed when the lattice is compressed from different ends, as indicated in Fig. 5a. We further quantify the distinct capacity for energy absorption by using

$$\beta = \frac{|W_{\mathrm{P}} - W_{\mathrm{Q}}|}{W_{\mathrm{P}} + W_{\mathrm{Q}}}. \tag{16}$$

The experimental and FEM results are plotted in Fig. 5c, where we observe that the energy absorption capacity in positive direction is more than 1.5 times larger (EXP) than that in the negative position.

Now we move to investigate the elastic modulus derived along opposite loading directions. Here the nonlinear elastic modulus is expressed as $E = \sigma_z\,(1+\varepsilon_z)/\ln(1+\varepsilon_z)$, where $E_{\mathrm{P}\to\mathrm{Q}}$ and $E_{\mathrm{Q}\to\mathrm{P}}$ denote the Young's modulus in the loading directions corresponding to $\mathrm{P} \to \mathrm{Q}$ and $\mathrm{Q} \to \mathrm{P}$, respectively. To give a more vivid physical description, we choose $E_{\mathrm{Q}\to\mathrm{P}}/E_{\mathrm{P}\to\mathrm{Q}}$ to reveal the contrast of elastic constants along opposite directions. In Fig. 5a, we have observed different reaction forces for an input compressive displacement upon switching the applied loading direction, which indicates directional elastic modulus. This behavior is further validated by the results shown in Fig. 6a, where the elastic modulus in the positive direction is at least two times larger than that in the negative direction, and $E_{\mathrm{Q}\to\mathrm{P}}/E_{\mathrm{P}\to\mathrm{Q}} > 1$ is observed throughout the compression process. Besides, the elastic modulus is not a constant, but robustly depends on both the magnitude and the direction of the applied load. This indicates a nonlinear and robustly tunable elastic modulus for the proposed metamaterials. With the increment of compressive strains, $E_{\mathrm{Q}\to\mathrm{P}}/E_{\mathrm{P}\to\mathrm{Q}}$ increases and then gradually decreases. The change in variation trend is mainly attributed to the configuration transition in the loading conditions $F_{\mathrm{P}}$. Actually, the compression–buckling pattern in tilt connectors turns to stretching–bending as the compression increases, whereas the latter

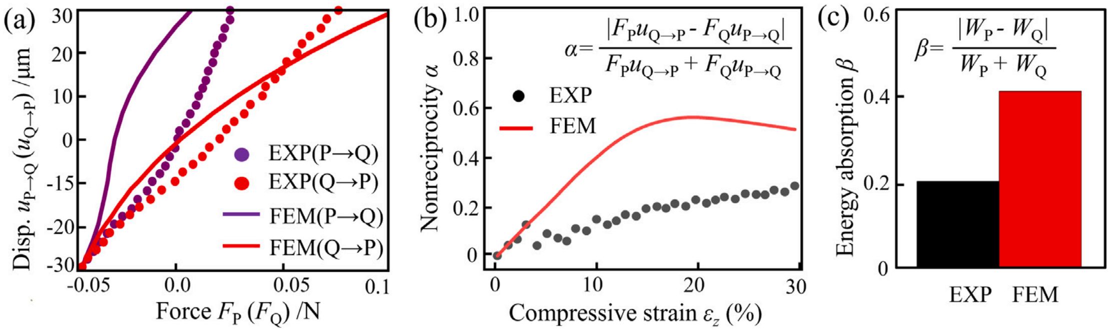


**Fig. 5.** Demonstration of the non-reciprocal mechanical behavior. (a) Simulated and experimental results for force–displacement responses are depicted by curves and dots, respectively. (b) Deformation non-reciprocity $\alpha$ is plotted as the function of compressive strain. (c) Asymmetrical behavior in energy absorption capacity $\beta$ is obtained and presented from experimental and FEM results, respectively.

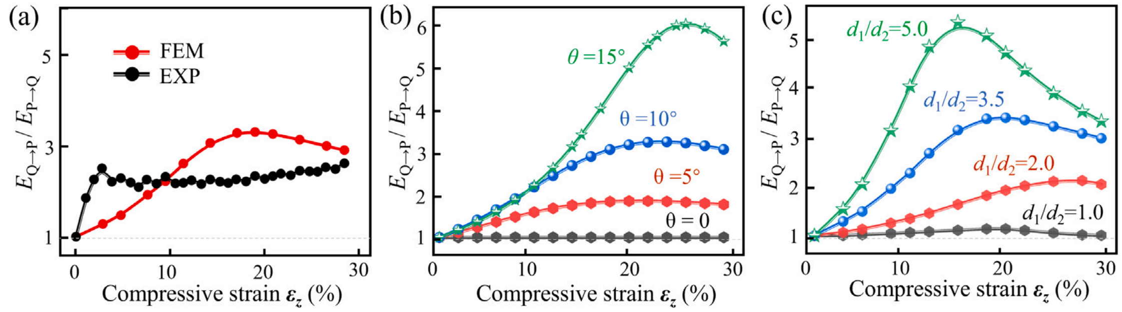


**Fig. 6.** Asymmetrical elastic behaviors. (a) Variations of the nonlinear elastic modulus indicated by $E_{Q\to P}/E_{P\to Q}$. Simulated and experimental results are depicted in red and black, respectively. Structural geometry effects on the asymmetrical elastic modulus: (b) tilt angles and (c) diameter ratio. The parameter analysis results are obtained from FEM analysis.

pattern dominates the tilt connector during the whole compression process in the loading conditions $F_Q$. This indicates that the structural deformation turns out to be consistent, hence the deformation contrast (accordingly the non-reciprocity) is reduced.

Given the match between FEM analysis and experiments (Fig. 5), we then investigate the structural geometry effects on the nonlinear elastic modulus by FEM. When the metamaterial lattice is loaded from opposite ends, the microstructures exhibit asymmetrical deformations. This difference in deformation patterns results in the contrast in mechanical behavior and generates high non-reciprocity. Intuitively, the tilt angle $\theta$ is the nonreciprocity indicator to be considered. Therefore, we construct metamaterial lattices with different tilt angles, i.e., 0°, 5°, 10°, and 15°, as shown in Fig. 6b. All loading conditions are the same as those employed in the experiments. Identical elastic moduli are obtained along opposite directions when the tilt angle is $\theta = 0$, where symmetrical structures are recovered. In such cases, the structure is mirror-symmetric, from which its response immediately follows mirror-symmetric behavior. The elastic modulus is constant and independent of both the magnitude and direction of the applied load. As the tilt angle increases, $E_{Q\to P}/E_{P\to Q}$ is noticeably increased by approximately 500% (from 1 to 5.9), due to an increase in the tilt angle $\theta = 0\to 15°$.

The asymmetrical deformation of tilt connectors plays the key role in producing mechanical non-reciprocity. However, in the deformation configurations, we observe buckling of the main beam, which is not desired for the proposed metamaterials. Here, the effect of beam diameters ($d_1/d_2$) on the elastic modulus is studied. Generally, a larger value of $d_1/d_2$ denotes stronger resistance to buckling of the main beam and less impact on the designed non-reciprocity behavior. As shown in Fig. 6c, the nonlinear elastic modulus ratio $E_{Q\to P}/E_{P\to Q}$ is observed increasing due to the increment of beam diameters $d_1/d_2$. Specifically, the maximum value of $E_{Q\to P}/E_{P\to Q}$ is increased by approximately 350%, from 1.13 (for geometry size $d_1/d_2 = 1.0$) to 5.13 (for geometry size $d_1/d_2 = 5.0$).

As depicted above, the asymmetrical elastic behavior of the proposed metamaterial lattices can be tailored by changing the beams' diameter ($d_1, d_2$) and tilt angles ($\theta$). Mechanical characters can be also tuned by the magnitude and direction of applied load. This will pave broad avenues and offer much flexibility in tailoring mechanical propagation and energy absorption.

### *3.3. Tunable band structures*

We then investigate band structures of the non-reciprocal mechanical metamaterials. As discussed above, the proposed metamaterial shows different elastic constants depending on the loading direction and strain, behaving like different materials. Here, we highlight a potential application to tunable phononic band gap structures. It is well-known that the dispersion of elastic waves

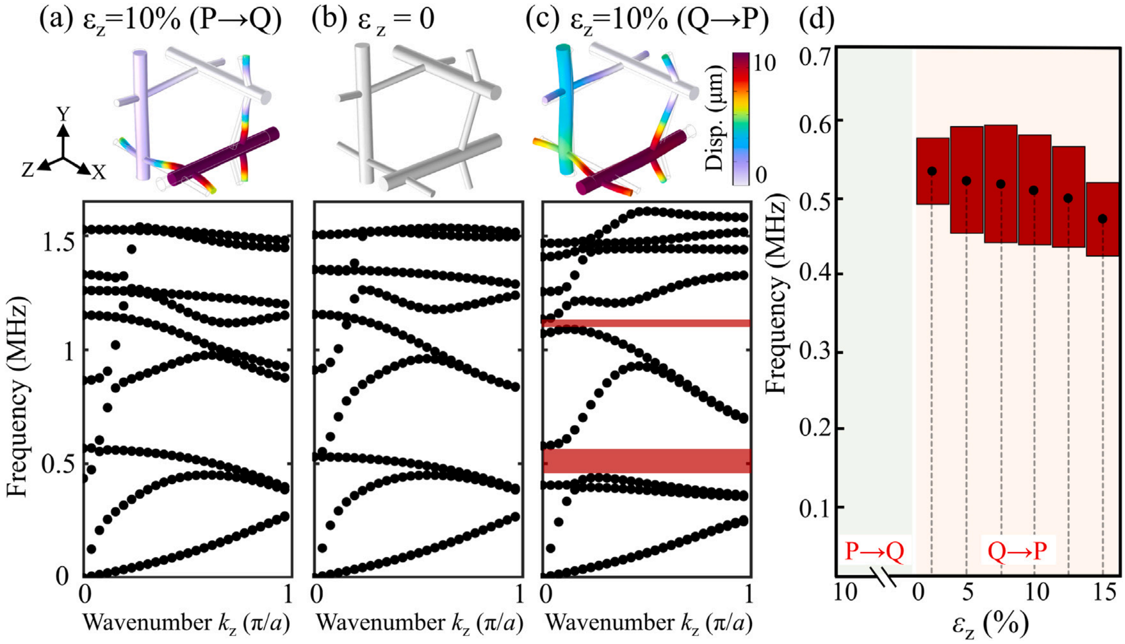


**Fig. 7.** The band structure for elastic waves propagating along $z$-direction for different configurations. The applied strains are (a) 10%(P → Q), (b) 0 and (c) 10%(Q → P), respectively. We mention in passing that the structure is pushed on different sides, rather than pulling-pushing on one side. The band gaps are highlighted in red. (d) The frequency range of the first band gap is plotted as a function of the pre-displacement.

is highly dependent on the density and the modulus of materials. The direction-sensitive deformation pattern of the metamaterial gives rise to different configurations and elongation, and thus causes a modulation of the volume. This leads to modulated relative density since the overall mass is conserved. The load-dependent variations of Young's modulus further contribute to the change of the dispersion relation. The phononic band structure for elastic waves propagating in the $z$ direction is shown in Fig. 7. We realize that geometry parameters (e.g., the diameter of beams) will certainly play a role in band structures following the principle of local resonance. Herein, the diameter $d_1 = 11$ μm is employed to elevate the first band gap discrepancy upon different loading directions. The essential fact is that the selected parameter is to optimize the metamaterial's dynamic characteristics without affecting its static mechanical properties. The band structures can certainly be further optimized, but are not further discussed here.

As apparent in Fig. 7d, the first band gap of the structure appears in the range between 454 kHz and 589 kHz when a strain of 5% is applied along the $z$ direction. It does not shift significantly with the applied strain, as exemplified by the right panel where the strain increases gradually to 15%. Besides, the size of the band gap does change as a result of the reconfiguration process, but such variations are not significant. However, we demonstrate a tunable band gap dependent on both the direction and magnitude of external mechanical stimulus. This phenomenon is consistent with our previously designed mechanical metamaterials (Dudek et al., 2023). We find that the band structure is deformed in an asymmetrical manner, as distinct band gap characteristics are induced for the metamaterial when external loads of the same magnitude but opposite direction are applied. Specifically, "transmission" or "prohibition" of an elastic wave (in a certain frequency range) can be flexibly tuned by simply switching the direction of applied loads.

If we switch the direction of applied strains, i.e., to the loading conditions $F_P$, no band gap is observed. The metamaterials present distinct band gap characteristics under different loading directions $F_Q$ and $F_P$. This contrast indicates that elastic waves can propagate or be prohibited through the mechanical metamaterials by tuning the direction of applied mechanical strains. The results show that without rebuilding the system, the transition of geometry configurations can be tailored to actively control the formation of band gaps, which benefits the design of vibration dampers and sensors. Potential applications of the developed metamaterials are listed. First, elastic wave dispersion relies on both the applied strain and the original geometry, implying a high degree of design flexibility. Second, even after the structure is fabricated, its wave propagation property is not fixed but can be changed without rebuilding it. Various dispersion properties can be tuned and tailored only via external mechanical excitation, which reduces the operation requirements to obtain adjustable dispersion behaviors.

## 4. Conclusion

In this work, we have proposed 3D mechanical metamaterials possessing tailorable non-reciprocal elastic modulus, asymmetrical deformation, and direction-dependent energy absorption capacity. By suitably designed asymmetries, the metamaterial displays strong non-reciprocity for static applied forces. The resulted elastic modulus is not a material constant, but dependent on both the magnitude and direction of the applied load. Furthermore, the nonlinear elastic modulus can be tailored by changing the tilt angle and diameter ratio: it is increased approximately by 200% (from 1 to 3), due to an increase in the tilt angle $\theta = 0 \rightarrow 30°$, and is elevated by approximately 350%, from 1.13 (for geometry size $d_1/d_2 = 1.0$) to 5.13 (for geometry size $d_1/d_2 = 5.0$). An obvious contrast in the band structures of elastic waves is also demonstrated, i.e., band gaps are formulated when the metamaterial is loaded from one direction, while no band gap appears when the structure is loaded from another direction. Therefore, one can transmit or prohibit the propagation of elastic waves (in a certain frequency range) by simply changing the direction of applied loads. The proposed metamaterial paves a feasible way to realize static one-way functionalities, and can find potential applications in impact energy absorption, low-frequency vibration attenuation, and so forth.

## CRediT authorship contribution statement

**Qingxiang Ji:** Writing – original draft, Formal analysis, Conceptualization. **Jinliang Wang:** Software, Methodology, Formal analysis. **Brahim Lemkalli:** Writing – review & editing, Investigation, Data curation. **Gwenn Ulliac:** Resources. **Changguo Wang:** Validation, Supervision, Project administration. **Sébastien Guenneau:** Writing – review & editing, Methodology. **Muamer Kadic:** Writing – review & editing, Validation, Supervision, Methodology.

## Declaration of competing interest

The authors declare that they have no known competing financial interests or personal relationships that could have appeared to influence the work reported in this paper.

## Acknowledgments

Q.J. acknowledges support by the European Union under Marie Skłodowska-Curie Actions Postdoctoral Fellowships [No. 101149710] and by the National Natural Science Foundation of China [Nos. 12302169, 12172102], M.K. acknowledges support by the ANR PNanoBot [ANR-21-CE33-0015] and ANR OPTOBOTS project [ANR-21-CE33-0003].

## Data availability

All the data supporting the conclusions of this study are included in the article.

## References

Achenbach, J.D., 2003. Reciprocity in Elastodynamics. Cambridge University Press.
Attarzadeh, M., Maleki, S., Crassidis, J., Nouh, M., 2019. Non-reciprocal wave phenomena in energy self-reliant gyric metamaterials. J. Acoust. Soc. Am. 146 (1), 789–801.
Attarzadeh, M., Nouh, M., 2018. Non-reciprocal elastic wave propagation in 2D phononic membranes with spatiotemporally varying material properties. J. Sound Vib. 422, 264–277.
Chen, X., Ji, Q., Martinez, J.A.I., Tan, H., Ulliac, G., Laude, V., Kadic, M., 2022a. Closed tubular mechanical metamaterial as lightweight load-bearing structure and energy absorber. J. Mech. Phys. Solids 167, 104957.
Chen, X., Moughames, J., Ji, Q., Martínez, J.A.I., Tan, H., Ulliac, G., Laude, V., Kadic, M., 2022b. 3D lightweight mechanical metamaterial with nearly isotropic inelastic large deformation response. J. Mech. Phys. Solids 169, 105057.
Chen, T., Pauly, M., Reis, P.M., 2021. A reprogrammable mechanical metamaterial with stable memory. Nature 589 (7842), 386–390.
Coulais, C., Sounas, D., Alu, A., 2017. Static non-reciprocity in mechanical metamaterials. Nature 542 (7642), 461–464.
Dong, L., Zhou, K., Wang, D., 2024. Programmable nonreciprocal poynting effect enabled by lattice metamaterials. Sci. Adv. 10 (24), eadl5774.
Dudek, K.K., Iglesias Martínez, J.A., Ulliac, G., Hirsinger, L., Wang, L., Laude, V., Kadic, M., 2023. Micro-scale mechanical metamaterial with a controllable transition in the Poisson's ratio and band gap formation. Adv. Mater. 35 (20), 2210993.
Florijn, B., Coulais, C., van Hecke, M., 2014. Programmable mechanical metamaterials. Phys. Rev. Lett. 113 (17), 175503.
Frenzel, T., Kadic, M., Wegener, M., 2017. Three-dimensional mechanical metamaterials with a twist. Science 358 (6366), 1072–1074.
Hu, Z., Wei, Z., Wang, K., Chen, Y., Zhu, R., Huang, G., Hu, G., 2023. Engineering zero modes in transformable mechanical metamaterials. Nat. Commun. 14 (1), 1266.
Ji, Q., Moughames, J., Chen, X., Fang, G., Huaroto, J.J., Laude, V., Martínez, J.A.I., Ulliac, G., Clévy, C., Lutz, P., et al., 2021. 4D thermomechanical metamaterials for soft microrobotics. Commun. Mater. 2 (1), 93.
Kadic, M., Milton, G.W., van Hecke, M., Wegener, M., 2019. 3D metamaterials. Nat. Rev. Phys. 1 (3), 198–210.
Lamb, H., 1887. On reciprocal theorems in dynamics. Proc. Lond. Math. Soc. 1 (1), 144–151.
Li, B., Ji, Q., Wang, J., Wang, C., Kadic, M., 2024. Thermal conductivity and nonreciprocity in wrinkled monolayer graphene ring. Thin-Walled Struct. 195, 111523.
Li, S., Lerch, M.M., Waters, J.T., Deng, B., Martens, R.S., Yao, Y., Kim, D.Y., Bertoldi, K., Grinthal, A., Balazs, A.C., et al., 2022. Self-regulated non-reciprocal motions in single-material microstructures. Nature 605 (7908), 76–83.
Li, X., Peng, W., Wu, W., Xiong, J., Lu, Y., 2023. Auxetic mechanical metamaterials: from soft to stiff. Int. J. Extrem. Manuf. 5 (4), 042003.
Librandi, G., Tubaldi, E., Bertoldi, K., 2021. Programming nonreciprocity and reversibility in multistable mechanical metamaterials. Nat. Commun. 12 (1), 3454.
Montazeri, A., Rahimi, M., Park, H.S., 2025. Non-reciprocity and asymmetric elasticity in twisting chiral metamaterials. Int. J. Mech. Sci. 109990.
Nadkarni, N., Arrieta, A.F., Chong, C., Kochmann, D.M., Daraio, C., 2016. Unidirectional transition waves in bistable lattices. Phys. Rev. Lett. 116 (24), 244501.
Nassar, H., Yousefzadeh, B., Fleury, R., Ruzzene, M., Alù, A., Daraio, C., Norris, A.N., Huang, G., Haberman, M.R., 2020. Nonreciprocity in acoustic and elastic materials. Nat. Rev. Mater. 5 (9), 667–685.
Ni, X.H., Teng, X.C., Jiang, W., Zhang, Y., Ren, X., 2024. Multi-objective optimization and theoretical analysis of re-entrant structure with enhanced mechanical properties. Thin-Walled Struct. 111791.

Pai, P.F., Nayfeh, A.H., 1994. A fully nonlinear theory of curved and twisted composite rotor blades accounting for warpings and three-dimensional stress effects. Int. J. Solids Struct. 31 (9), 1309–1340.
Pai, P., Palazotto, A., 1996. Large-deformation analysis of flexible beams. Int. J. Solids Struct. 33 (9), 1335–1353.
Palermo, A., Celli, P., Yousefzadeh, B., Daraio, C., Marzani, A., 2020. Surface wave non-reciprocity via time-modulated metamaterials. J. Mech. Phys. Solids 145, 104181.
Reis, P.M., López Jiménez, F., Marthelot, J., 2015. Transforming architectures inspired by origami. Proc. Natl. Acad. Sci. 112 (40), 12234–12235.
Shaat, M., 2020. Nonreciprocal elasticity and the realization of static and dynamic nonreciprocity. Sci. Rep. 10 (1), 21676.
Shaat, M., Moubarez, M., Khan, M., Khan, M., Alzo'ubi, A., 2020. Metamaterials with giant and tailorable nonreciprocal elastic moduli. Phys. Rev. Appl. 14 (1), 014005.
Shaat, M., Park, H.S., 2023. Chiral nonreciprocal elasticity and mechanical activity. J. Mech. Phys. Solids 171, 105163.
Surjadi, J.U., Gao, L., Du, H., Li, X., Xiong, X., Fang, N.X., Lu, Y., 2019. Mechanical metamaterials and their engineering applications. Adv. Eng. Mater. 21 (3), 1800864.
Süsstrunk, R., Huber, S.D., 2015. Observation of phononic helical edge states in a mechanical topological insulator. Science 349 (6243), 47–50.
Trainiti, G., Ruzzene, M., 2016. Non-reciprocal elastic wave propagation in spatiotemporal periodic structures. New J. Phys. 18 (8), 083047.
Wang, X., Li, Z., Wang, S., Sano, K., Sun, Z., Shao, Z., Takeishi, A., Matsubara, S., Okumura, D., Sakai, N., et al., 2023a. Mechanical nonreciprocity in a uniform composite material. Science 380 (6641), 192–198.
Wang, P., Lu, L., Bertoldi, K., 2015. Topological phononic crystals with one-way elastic edge waves. Phys. Rev. Lett. 115 (10), 104302.
Wang, L., Martínez, J.A.I., Ulliac, G., Wang, B., Laude, V., Kadic, M., 2023b. Non-reciprocal and non-Newtonian mechanical metamaterials. Nat. Commun. 14 (1), 4778.
Wang, M., Yi, K., Kovacic, I., Zhou, X., Zhu, R., 2025. Ultralow-frequency absorption mechanism of a hybrid membrane resonator with acoustic soft boundary condition. J. Sound Vib. 596, 118686.
Xu, M., Yamamoto, K., Puebla, J., Baumgaertl, K., Rana, B., Miura, K., Takahashi, H., Grundler, D., Maekawa, S., Otani, Y., 2020. Nonreciprocal surface acoustic wave propagation via magneto-rotation coupling. Sci. Adv. 6 (32), eabb1724.
Zhang, P., Chen, X., Yu, P., Zhao, K., Ma, H., Liu, S., Tan, H., Laude, V., Kadic, M., 2025. Grid hollow octet truss lattices that are stable at low relative density. J. Mech. Phys. Solids 197, 106068.
Zhang, Z., Delplace, P., Fleury, R., 2021. Superior robustness of anomalous non-reciprocal topological edge states. Nature 598 (7880), 293–297.
Zhang, Y., Zhong, J., Zhao, Z., Bai, R., Yin, Y., Yu, Y., Li, B., 2024. Mechanical janus lattice with plug-switch orientation. Theor. Appl. Mech. Lett. 14 (1), 100493.